

# Defect depth retrieval method based on nonlinear transformation for pulsed thermographic inspection

Meiling Wang, Bin Gao<sup>\*</sup>, Tongle Wu, Bozhen Hu, Li Liu

School of Automation Engineering, University of Electronic Science and Technology of China, Chengdu, China

## ARTICLE INFO

### Keywords:

Carbon fiber reinforced polymer  
Optical pulsed thermography  
Gaussianization transform  
Defect depth

## ABSTRACT

The carbon fiber reinforced polymer (CFRP) has been widely used in the aerospace field. During its utilization under the severe environment, CFRP is prone to defects, including impacts, debonds, delaminations, and cracks. Optical pulsed thermography (OPT) nondestructive testing has been used for qualitative and quantitative analysis of such defects. This paper proposes the nonlinear transfer model of peak contrast time analysis to determine defect depth by using OPT technology. The mechanism of the nonlinear relationship between peak contrast time and defect depth is demonstrated and validated by experiments. To effectively predict the defect depth, gaussianization transform is modeled as a nonlinear conversion in defects depth determination. The results of the experiments have indicated that the proposed method has significantly enhanced the accuracy in depth determination.

## 1. Introduction

Carbon fiber reinforced composites (CFRP) are widely used in various fields of military and civil industry because of their excellent properties such as low density, high-temperature resistance, high strength and oxidation resistance [1–4]. For laminated composite materials, repeated cyclic stresses and impact will cause quality problems as well as defects, which include delamination, debonding, crack and impact [5]. Thus, non-destructive testing and evaluation (NDT&E) techniques are essential to ensure safety, reliability and operational life.

At present, the main non-destructive testing methods for composite materials are ultrasonic testing [6,7], X-ray [8,9], eddy current [10,11], microwave [12], resistance measurement [13], acoustic emission [14, 15], laser speckle method [16], infrared thermography (IRT) [17,18] and Holographic interferometry (HI) [19,20]. These technologies have some shortcomings. Table 1 summarizes the shortcomings of non-destructive testing for CFRP.

In the past 20 years, with the rapid development of thermal imagery and hardware devices in measuring two-dimensional temperature field, infrared thermography has become a more reliable non-destructive testing method. IRT has many advantages [21] as it is a real-time, non-contact imaging technology that has no harmful effects and can be easily made automatically. Many different heat excitation sources are used in infrared detection, such as optics [22], ultrasound [23],

microwave [24] and eddy-current [25]. Optical pulsed Thermography (OPT) is an effective detection method in the detection of composite materials. Chulkov et al. [26] have compared different optical sources for NDT, such as Xenon flash lamps, halogen lamps and LED.

In the research of Optical pulsed thermography, the data processing algorithm is not only used to improve the detection level of IRT technology, but also to characterize the defects in order to realize the automation of the detection process [27]. Principal component analysis (PCA) and Thermographic signal reconstruction (TSR) are relatively helpful processing algorithms for improving qualitative detection results [28]. Although these algorithms are helpful for the detection assessments of composite materials whereas they may not be sufficient enough for quantitative study in depth prediction of the defects. In addition, Pulsed phase thermography (PPT) is a technique of inversion of the depth based on the equation of the thermal diffusion length [29]. Thus, quantitative NDE analysis remains a challenging task in anisotropic materials for OPT.

In recent years, several methods estimate the defect depth by using a characteristic time [30,31]. The first proposed and the most commonly used method utilizes the time point when the maximum thermal contrast between a defective and a sound reference point occurs, known as Peak Contrast Time [32–34]. It was found that the peak contrast time is approximately proportional to the square of the defect depth [35]. Krapez et al. [36] proposed the time point on the temperature-time

<sup>\*</sup> Corresponding author.

E-mail address: [bin\\_gao@uestc.edu.cn](mailto:bin_gao@uestc.edu.cn) (B. Gao).

**Table 1**  
Disadvantages of composite non-destructive testing technology.

Technique	problem
ultrasonic testing	Need a coupling agent, Difficult to achieve non-contact detection
X-ray	Insensitive to layered defects, Radiation is harmful, Complex system and high cost
eddy current	Workpiece geometry and lift-off effects have a large impact, and it is difficult to quantify defects.
laser speckle method	The detection depth is small, it is difficult to find internal defects
acoustic emission	Low detection sensitivity and low resolution
Holographic interferometry (HI)	Complex implementation conditions

curve is the moment when the temperature signal above the defects diverges from the reference signal. Due to the noise effect in thermal data, the establishment of a threshold level is required to identify the time point on the temperature-time curve [37]. Ringermacher et al. [38] suggested to use the slope or first derivative of the temperature contrast to determine the defect depth. Theodorakeas et al. [39] performed quantitative analysis in both the temporal and frequency domains. These are parameters of thermal contrast peak slope time and blind frequency. It was observed that frequency domain analysis presents greater accuracy. Shepard et al. [40] proposed the peak time of the second derivative of temperature decay in the logarithmic scale, which is called the Log Second Derivative (LSD) method. The second derivative peak time appears earlier and it is less affected by three-dimensional thermal diffusion. Sun [41] introduced Least-Square Fitting Method for depth prediction based on a theoretical heat transform model. Zhao [42] proposed a Nonlinear System Identification (NSI) method to measure the defect depth in a more automatic and flexible manner. In the study of dynamic thermal tomography (DTT), Wei et al. [43] directly made linear fitting curves of peak contrast time and defect depth  $d$  to estimate depth. Omar et al. [44] applied infrared self-referencing thermography based on peak contrast time to establish depth maps.

Although the above research methods have made considerable progress in thermography defect prediction, the commonly used algorithms still have limitations in accurately measuring defect depth due to weak modeling, complex interference and etc. In this paper, the nonlinear transfer model of peak contrast time analysis is proposed to determine defect depth. The mechanism of nonlinear relationship between peak contrast time and defect depth is demonstrated and validated by experiments. To effectively predict the defect depth, gaussianization transform is modeled as a nonlinear conversion in defects depth determination.

The remaining portion of this paper is organized as follows. Section 2

introduces the methodology of OPT and gaussianization transform. Section 3 describes the experimental setup and discusses experimental results and analysis. Finally, section 4 reports conclusions and perspectives of further developments.

## 2. Methodology

### 2.1. Pulsed thermographic inspection

In pulsed thermographic inspection, high-power flash lamps or halogen lamps are used to heat the sample. Heat conduction then conducts from the surface to the interior of the sample, leading to a continuous decrease of the temperature. The thermophysical properties of the defect area affect the heat conduction, causing a temperature deviation between the defective and the sound areas. A thermal imaging camera controlled by a PC records the temperature change and the system of the optical pulsed thermography is shown in Fig. 1.

Temperature variation at  $z$  from the inner surface of the specimen is expressed as follow

$$T(z, t) = \frac{Q}{\sqrt{\pi\rho ckt}} \exp\left(-\frac{z^2}{4at}\right) \quad (1)$$

where  $Q$  is the input energy,  $\rho$  is density,  $c$  is heat capacity,  $k$  is the thermal conductivity of the material (W/(K·m)) and  $\alpha$  is the thermal diffusivity ( $\frac{m^2}{s}$ ).

In the actual detection, the surface temperature of the specimen can only be obtained by infrared thermal imager. Temperature variation in the defect-free zone on the surface of the specimen can be expressed as

$$T_n(0, t) = \frac{Q}{\sqrt{\pi\rho ckt}} \quad (2)$$

If there exists a defect inside the specimen, the distance between the defect location and the surface is given as  $d$ . Temperature variation at the sound zone on the surface can be expressed as

$$T_d(0, t) = \frac{Q}{\sqrt{\pi\rho ckt}} \left(1 + 2 \exp\left(-\frac{d^2}{at}\right)\right) \quad (3)$$

The temperature contrast between defective and non-defective regions can be expressed as

$$\Delta T = T_d(0, t) - T_n(0, t) = \frac{2Q}{\sqrt{\pi\rho ckt}} \exp\left(-\frac{d^2}{at}\right) \quad (4)$$

By differentiating equation (4), the peak time of temperature contrast can be calculated as

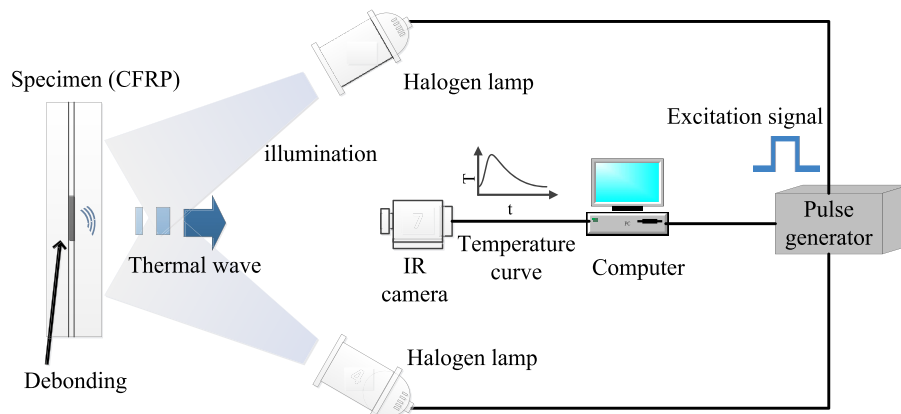


**Fig. 1.** Diagram of the optical pulsed thermography.

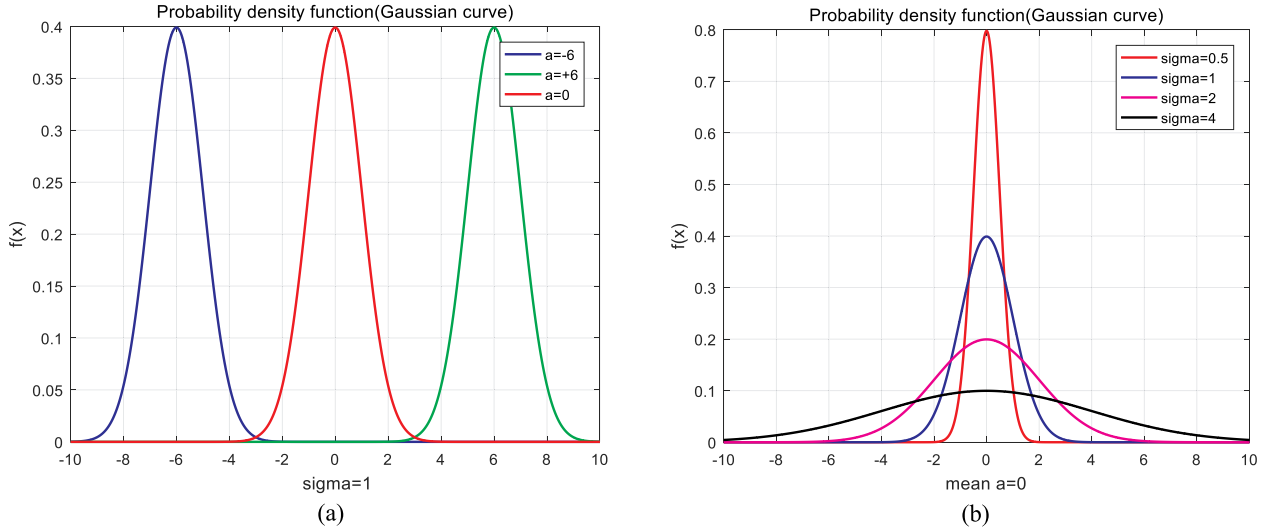


Fig. 2. Gaussian distribution(a) different mean and same  $\sigma$  (b) different  $\sigma$  and same mean.

$$t_{peak} = \frac{2d^2}{\alpha} \quad (5)$$

The above theoretical analysis is based on the standard PT approach with the flash lamp as an excitation source. In standard PT, the heating time is extremely short since it only lasts a few milliseconds. Thus, it can be approximately modeled as a Dirac's Delta function  $\delta(t)$ . It is difficult to achieve such short-time pulses if halogen lamps are used as the excitation source. Supposing the conditions hold the property of linearity and time-invariance, the long pulse response can be modeled as a simple superposition of a series of impulse responses  $h(t, i, j)$ .

Assuming a time shift  $\tau$  of several milliseconds conduct to the  $\delta(t)$  as it becomes  $\delta(t - \tau)$ . The corresponding temperature response  $h(t - \tau, i, j)$  will not be the same as  $h(t, i, j)$  described above. This is because the sample needs to be cooled to the initial temperature (thermal equilibrium) for at least several tens of seconds after the  $\delta(t)$  excitation. The temperature of the sample is relatively high and uneven when  $\delta(t - \tau)$  pulse acts on it, which leads to the initial condition for solving one-dimensional heat conduction Eq. (7) as written as

$$T_{t-\tau}(x, y, z, t)|_{t=0} = \phi_{t-\tau}(x, y, z) \quad (6)$$

where  $\phi_{t-\tau}(x, y, z)$  is a function characterizing of the uneven temperature distribution of the sample.

However, for the  $\delta(t)$  pulse,  $\phi_t(x, y, z)$  in equation (6) is a constant  $T_0$ . It indicates that the solutions of the two types of pulses are different in Eqn. (7) as  $h(t - \tau, i, j)$  does not completely coincide with the response  $h(t, i, j)$ . Thus, this does not hold to the time-invariance system anymore.

$$\rho c \frac{\partial T}{\partial t} - \alpha \frac{\partial^2 T}{\partial z^2} = Q \quad (7)$$

This interprets that a long pulse response is not a simple superposition of a series of short-time impulse responses. The  $t_{peak}$  in Eq. (5) will shift in the long pulse when using halogen lamps. Therefore, Eq. (5) cannot fit the actual situation and cannot be directly used to predict the depth. The duration of the long pulse is usually set in a few seconds as it is not fixed value due to the different test samples. Since in the testing of CFRP, the "pulse" is actually steady-state heating of a long pulse duration due to the low conductivity of the CFRP. The various durations of a long pulse will not cause an obvious shift of the  $t_{peak}$ . To validate this, the duration of 4s and 3s were set in the two experiments.

## 2.2. The proposed method in depth estimation

The above analysis simplifies the object to a one-dimensional heat

conduction model. Actually, this time determination will be affected by three-dimensional thermal diffusion. In addition, the temperature contrast  $\Delta T$  does not only depend on the depth of defect, but also on the lateral size of the defect because of the three-dimensional heat conduction as well as the excitation duration. Especially for composite materials, the anisotropic properties make us have to consider heat conduction in both x and y directions.

From equation (5), it is clear that the defect depth  $d$  has a nonlinear relation with  $t_{peak}$ , referred to as  $\tau_m$ . Consider the shift  $\tau_m$  caused by halogen lamps and the effects of three-dimensional heat conduction. Thus, the complex non-linear model between  $d$  and  $\tau_m$  is difficult to be established.

Many studies [34,42] consider  $d$  or  $d^2$  and  $\tau_m$  as giving a linear relationship to determine the depth, namely

$$d = w^T \tau_m \quad (8)$$

However, these approaches do not consider the actual physical model whereas it ignores the nonlinear characteristic. The linear processing cannot accurately determine depth. The actual non-linear equation can be considered as

$$\hat{d}_i = A^T \tau_{mi} + \mu_i \quad (9)$$

In particular, nonlinear relation is difficult to be solved due to the difficulty of the depth determination. This paper proposes a nonlinear projection function to transform this nonlinear relationship into a linear projection.

Linear transformation regression has a wide range of applications in data analysis, many nonlinear models can be transformed into linear models for regression analysis. There are two types of linearization methods for nonlinear models. One is a linear model that can be linearized, and another is a nonlinear model that is not linearizable. For the first case, direct substitution, function transformation, and series expansion methods can be used. Models that cannot be linearized and it is expressed as

$$Y = w^T x + u \quad (10)$$

where  $Y$  is nonlinear,  $w^T x$  is linear. In this paper, we aim at finding a linear relationship

$$d_i = A^T \tau_{mi}' \quad (11)$$

where  $\tau_{mi}'$  is the corrected value

$$\tau_{mi}' = \tau_{mi} + \varepsilon_i \quad (12)$$

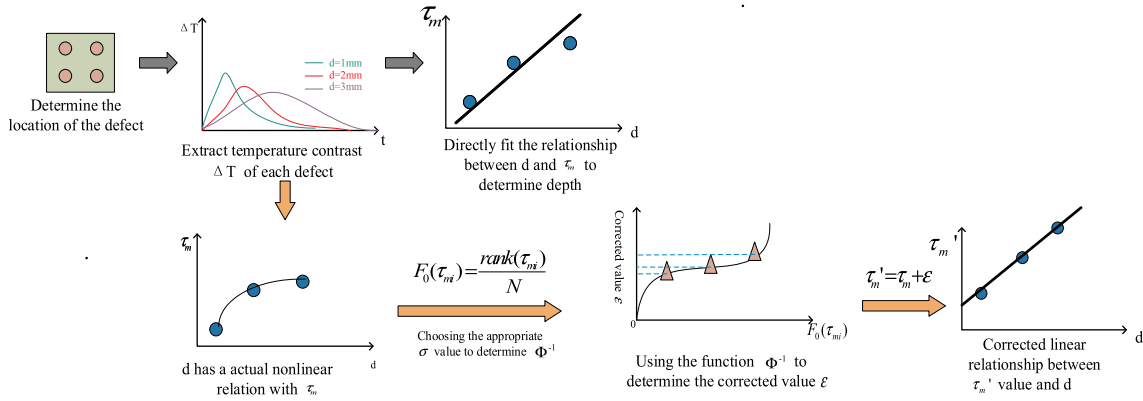


Fig. 3. The specific steps of depth determination by using gaussianization transform.

This paper proposes to use gaussianization transform to determine  $\varepsilon$ . Although the distribution of  $\varepsilon$  is uncertain, this uncertainty distribution can be accorded to a Gaussian distribution by a transformation.

The idea is to apply a smooth, invertible transformation to univariate data so that the distribution of the transformed data is approximated as Gaussian as possible. The reasons can be drawn as follows

1. It reduces the effect of outliers. Lots of real-world data exhibits long tails. For machine learning, the small number of examples in the tails of the distribution can have a large effect on results. Gaussianized data will “squeeze” the tails in towards the center.
2. Theoretical benefits. Gaussian distributions are well studied with many unique properties that it may like to leverage.
3. Various information-theoretic quantities are invariant under invertible transforms, so it makes sense to first transform into a friendlier distribution.

Gaussian distribution is an important probability distribution in the fields of mathematics, physics, and engineering. Gaussian distribution is often used to model noise and uncertainty. The mathematical form of the Gaussian distribution is as follows

$$\varphi(x) = \frac{1}{\sqrt{2\pi}\sigma} e^{-\frac{(x-a)^2}{2\sigma^2}} \quad (13)$$

where  $x$  is variable,  $a$  is mean,  $\sigma$  is a standard deviation. In Fig. 2, the expected value  $a$  of the normal distribution determines its position, and the standard deviation  $\sigma$  determines the magnitude of the distribution. Its CDF (accumulated distribution function) by  $\Phi$  that is:

$$\Phi(x) = \int_{-\infty}^x \varphi(t) dt \quad (14)$$

The form of the gaussianization transform is defined as Eqn. (15) [45].

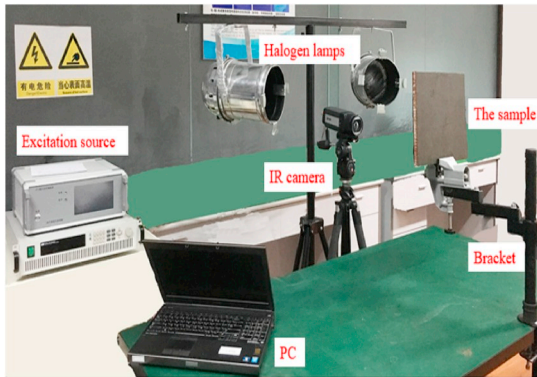
$$y_i = \Phi^{-1} \left( \frac{\text{rank}(x_i)}{N} \right), 1 \leq i \leq N \quad (15)$$

where  $\text{rank}(x_i)$  is the rank of  $x_i$  in the sorted list of samples. Since the CDF  $\Phi$  is a monotonically increasing function, it has an inverse  $\Phi^{-1}$ . In this paper, gaussianization transform  $y_i$  is used to denote uncertainty distribution  $\varepsilon$ ,  $x_i$  is the  $\tau_{mi}$  (the peak contrast time). Combining (11) with (12) and (15), we can obtain

$$d_i = A^T \left( \tau_{mi} + \Phi^{-1} \left( \frac{\text{rank}(\tau_{mi})}{N} \right) \right) \quad (16)$$

As can be seen from Fig. 2, the value of  $\sigma$  determines the magnitude of the Gaussian distribution, which determines  $\Phi^{-1}$  function. From equation (16), different degrees of correction can be made to the data by selecting different standard deviations. The specific steps are summarized as shown in Fig. 3.

From Fig. 3, traditional study directly fits the defect depth and peak contrast time directly into a linear projection. In the paper, considering the actual physical process, this nonlinear factor is considered as Gaussian distribution transformed from uncertainty distribution  $\varepsilon$  by using a gaussianization transform. Thus, this will make a more accurate linear projection between the defect depth and peak contrast time after correction.



(a)



(b)

Fig. 4. The platform of experiment: (a) excitation source of halogen lamps with a power of 2 KW and (b) excitation source of halogen lamps with a power of 3 KW.

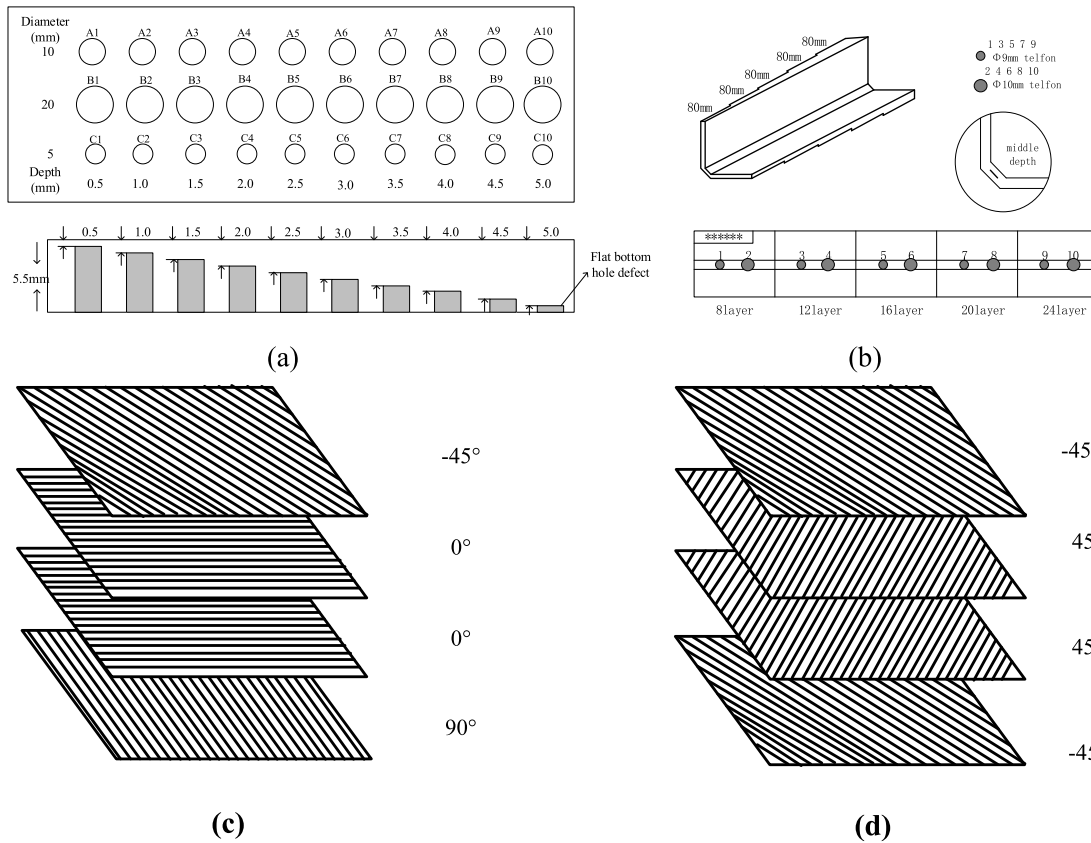


Fig. 5. Distribution of the defects in SP1 and SP2: (a) schematic diagram of the flat bottom hole defect locations in SP1(b) schematic diagram of embedded defect locations in SP2(c) ply orientation of SP1 (d) ply orientation of SP2.

### 3. Experimental results and analysis

#### 3.1. Experimental setup

##### 3.1.1. Experiment platform

An experimental platform of optical pulsed thermography (OPT) is shown in Fig. 4. Two kinds of excitation source of halogen lamps are used with a power of 2 kW and 3 kW, respectively. Both lamps locate in 80 cm from the specimen surface. Optical excitation source of ZY-B type has a maximum excitation power of 3 kW, and the voltage and current can be adjusted. ITECH IT6726G is adjustable with DC power. The IR camera is A655sc, with the resolution of 640x480 array and the thermal sensitivity is 0.05 °C. The wavelength ranges from 7.5 to 14 μm, and the sampling frequency ranges from 12.5 to 200, IR camera can be triggered by external or manual.

Two specimens were used for validation. The specimen 1(SP1) was a flat bottom hole specimen. The specimen 2(SP2) was designed by AVIC Chengdu Aircraft Industry Corporation.

The thickness in each layer of carbon fiber in SP1 is 0.25 mm. The fibers in each ply have a (-45°, 0°, 0°, 90°) stacking sequence in Fig. 5 (c). The defect of SP1 is a flat bottom hole defect as shown in Fig. 5(a). These defects were divided into 3 series (A-C in the schematic) where placed at different diameters ranging from 5 mm to 20 mm. Each series consisted of 10 defects of different depths (No.1 to No.10 in the schematic).

The SP2 is a R-type sample as shown in Fig. 5 (b). The debonding defect is made by artificial preset Teflon with a thickness of 0.1 mm. The defects are located in the bend. The thickness of each layer of carbon fiber in SP2 is 0.125 mm, with ply orientation of [-45/45/45/-45] s as shown in Fig. 5(d). The thickness of the specimen increases sequentially. These are 8-layers, 12-layers, 16-layers,20-layers,24-layers, respectively. Defects are embedded in the middle, that is, under the 4-layer

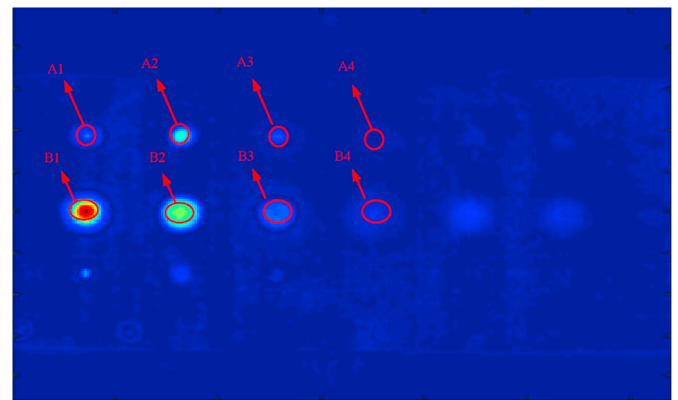


Fig. 6. Enhanced thermograms using structured sparse matrix decomposition.

(0.5 mm), 6-layer (0.75 mm), 8-layer (1.0 mm), 10-layer (1.25 mm) and 12-layer (1.5 mm) of CFRP.

#### 3.2. Result analysis

SP1 was tested by using a 3 kW excitation source. A heat pulse of 4s duration was deposited. Structured sparse matrix decomposition was used to enhance the contrast of the thermal image and the visibility of the defects. Fig. 6 shows the detection results.

To establish the temperature contrast, a reference temperature is required. Since the non-uniformity of the heat source, sound areas located near to the defect were selected. Fig. 7 (a) shows the temperature curves of the defective area and sound area, respectively. The temperature contrast is plotted in Fig. 7 (b).

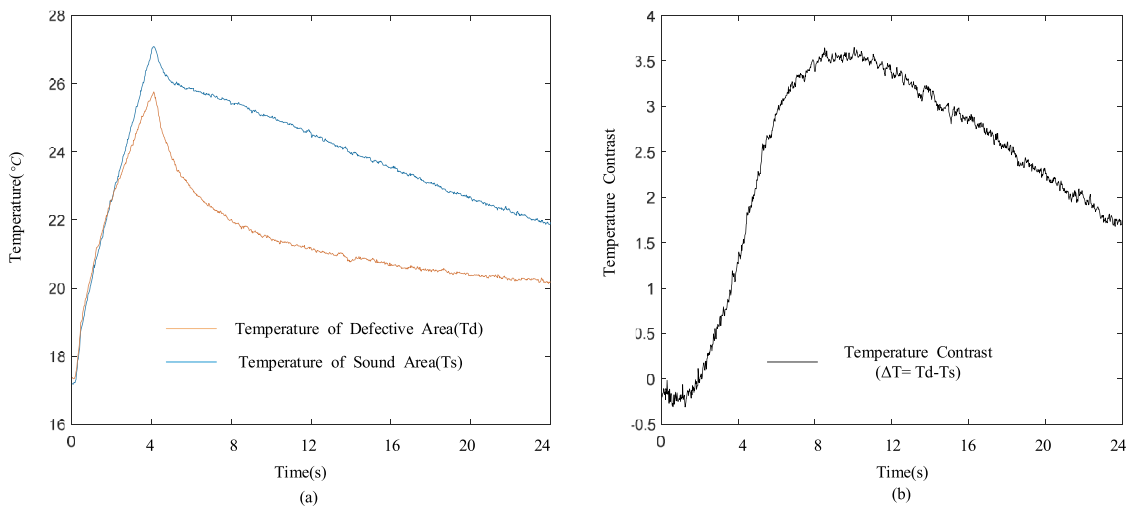


Fig. 7. Temperature curves and temperature contrast from the experimentally acquired thermogram for one of the defects.

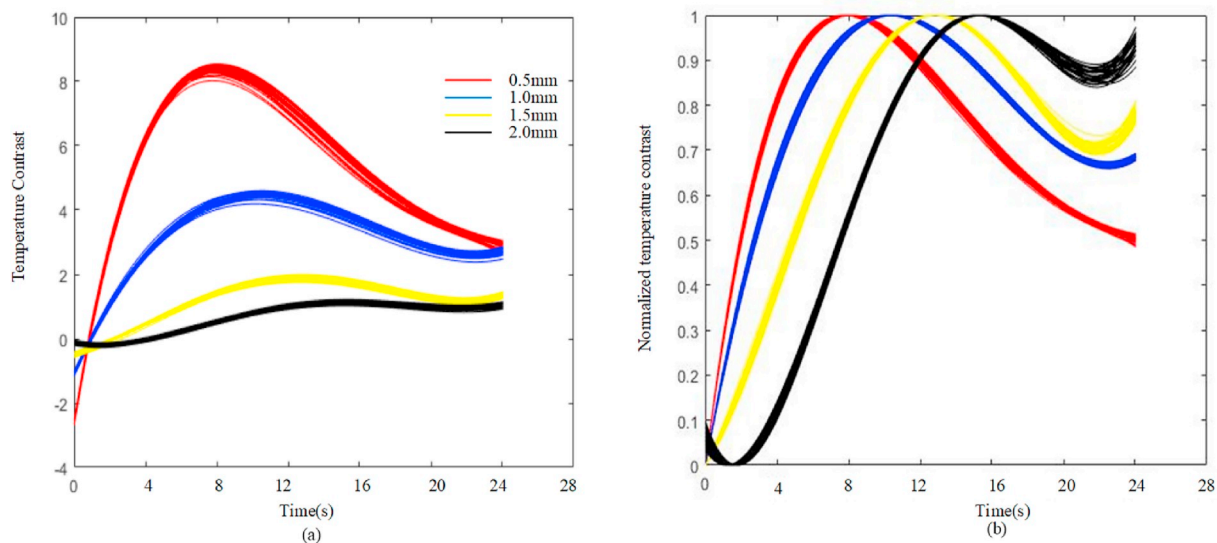


Fig. 8. (a) Temperature contrast of 20 mm diameter defects at different depths (b) Normalized temperature contrast of (a).

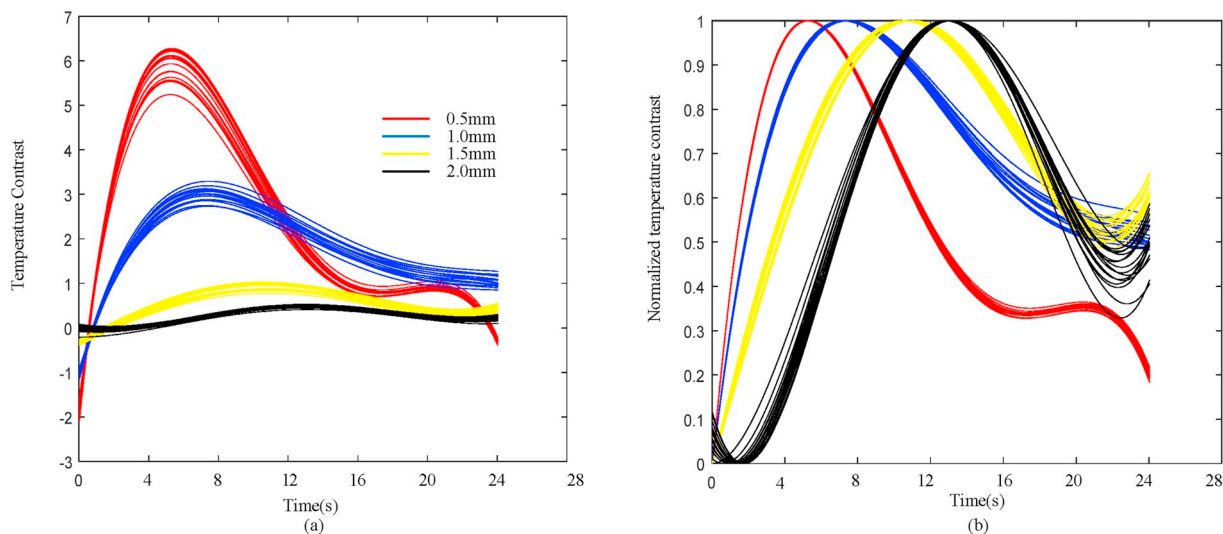


Fig. 9. (a) Temperature contrast of 10 mm diameter defects at different depths (b) Normalized temperature contrast of (a).

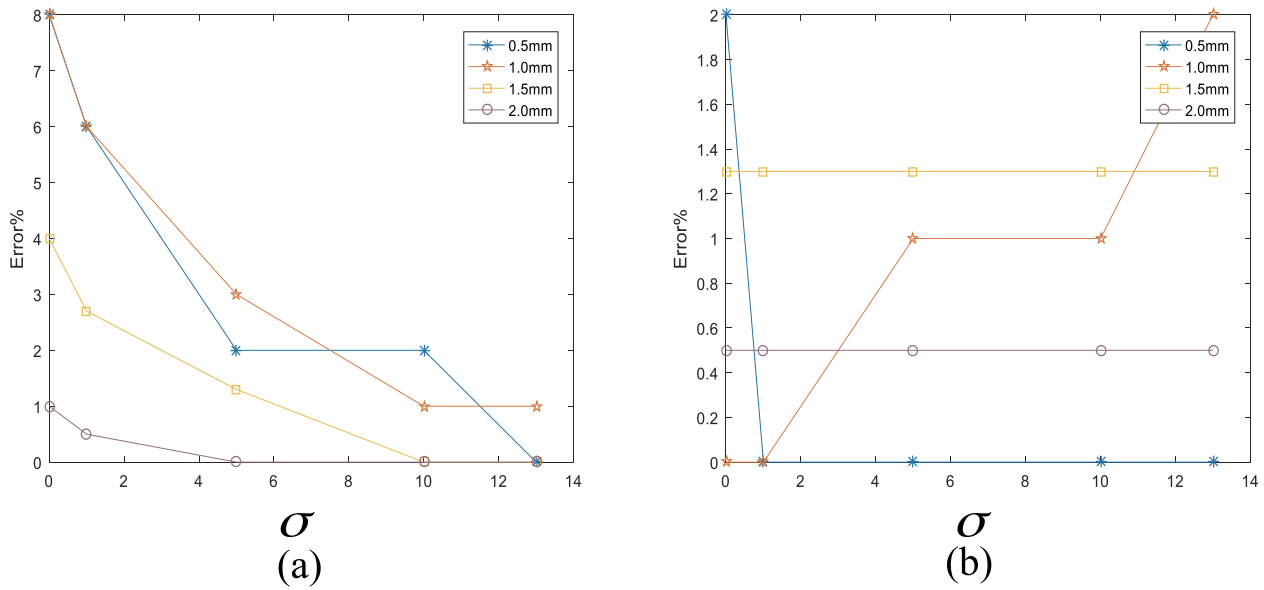


Fig. 10. (a) Depth prediction errors corresponding to different  $\sigma$  values with diameter of 10 mm(b) 20 mm.

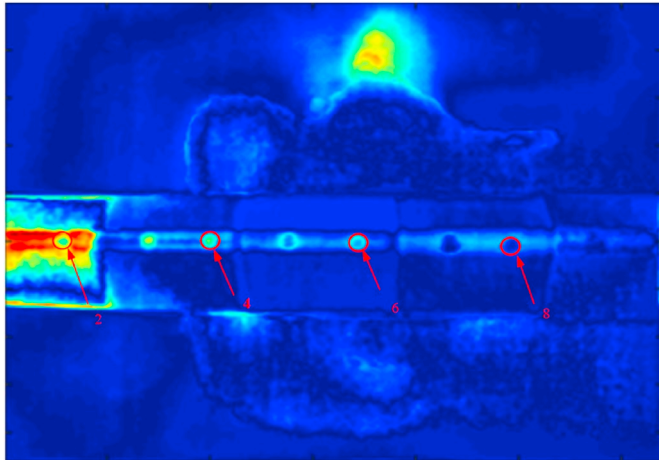


Fig. 11. Enhanced thermograms using structured sparse matrix decomposition.

Figs. 8 and 9 display the temperature contrast of each defect with a diameter of 20 mm and a diameter of 10 mm, where each bundle of curves corresponds to a different depth. As the depth of the defect

increases, the later the peak time of the temperature contrast curve appears. To observe the peak time more clearly, the temperature contrast is normalized.

The peak time of the temperature contrast was determined from the curves in Figs. 8 and 9, respectively. The goal is to modify the nonlinear relationship between the defect depth  $d$  and  $\tau_m$ .

The linear relationship between defect depth  $d$  and peak time  $\tau_m$  was compared before and after the correction of  $\tau_m$ . That is, the predicted depth results of Equation (9) and Equation (16) are compared. According to Equation (16), the choice of  $\sigma$  value will lead to different degrees of correction for  $\tau_m$ , thus having different depth prediction results.

The depth prediction errors before correction and the results after correction with different  $\sigma$  are shown in Fig. 10.  $\tau_m$  is not corrected when  $\sigma = 0$ . For the case of 10 mm-diameter defects, with the increase of  $\sigma$ , the error of each depth is getting small. In particular, the error changes more slowly as  $\sigma$  increases. When  $\sigma = 13$  the error of each depth is minimized. The prediction errors of depth at 0.5 mm, 1 mm, 1.5 mm and 2 mm can be reduced by 8%, 7%, 4%, and 1%, respectively. However, for defects with a diameter of 20 mm, the results are different. Defects with depths of 1.5 mm and 2 mm have no change in error with the change of  $\sigma$ . The errors are 1.3% and 0.5%, respectively. The prediction error is reduced from 2% to 0% at 0.5 mm depth. For defects of 1 mm depth, the error is instead increased. The error increases by 1% when

Table 2  
Comparison of pre-corrected depth estimates and corrected depth estimates.

Specimen	Diameter (mm)	Depth of defect (mm)	$\tau_m$ (s)	estimated depth (mm)/error before correction	$\sigma = 10$		improvement
					corrected d(mm)/error		
SP1	20 mm	0.5(B1)	6.91	0.51/2%	0.49/2%	0%	
		1.0(B2)	9.28	0.92/8%	1.00/0%	8%	
		1.5(B3)	13.22	1.61/7.3%	1.54/2.7%	4.6%	
		2.0(B4)	15.74	2.05/2.5%	1.99/0.5%	2%	
		2.5(B5)	17.82	2.41/3.6%	2.48/0.8%	2.8%	
	10 mm	0.5(A1)	5.17	0.60/20%	0.52/4%	16%	
		1.0(A2)	6.89	0.90/10%	0.99/1%	9%	
		1.5(A3)	10.26	1.48/1.3%	1.49/0.7%	0.6%	
		2.0(A4)	13.19	1.99/0.5%	1.97/1.5%	-1%	
		2.5(A5)	16.26	2.53/1.2%	2.53/1.2%	0%	
SP2	10 mm	0.5(2)	1.29	0.45/10%	0.48/4.0%	6%	
		0.75(4)	3.32	0.88/17.3%	0.78/4.0%	13.3%	
		1.0(6)	4.09	1.04/4.0%	1.00/0.0%	4%	
		1.25(8)	4.53	1.13/9.6%	1.24/0.8%	8.8%	

**Table 3**  
Network structure and parameters.

Layer (type)	Output Shape	Param.
Input layer	(B,1201)	0
Fully-connected layer	(B,801)	962802
Fully-connected layer	(B,534)	428268
Fully-connected layer	(B,356)	190460
Fully-connected layer	(B,237)	84609
Fully-connected layer	(B,158)	37604
Output layer	(B,1)	159

$\sigma = 3$ , and the error increases by 2% with  $\sigma = 13$ . This shows that there is no significant improvement in the value of smaller error itself. Since each defect in Fig. 10(a) has a slower change in error when  $\sigma > 5$ , and the error of 1 mm is increased when  $\sigma = 13$  in Fig. 10(b). The optimum value of  $\sigma$  should be 10.

To further confirm the optimality choice of  $\sigma = 10$  and comparing the corrected error results. An additional 2 kW excitation source experiment has been performed on SP1. The complicated R-type specimens SP2 was also tested using 3s long pulse durations. Defects selected in SP2 are larger diameter, numbered 2, 4, 6, 8 in Fig. 5(b), correspondingly marked in Fig. 11.

The comparison results are shown in Table 2. All defect errors in Table 2 are corrected within a 5% rate. For the defects with large errors, the correction results are greatly improved. For A1 and A2 defects of SP1, the original error is 20% and 10%, respectively. However, when  $\sigma = 10$ , the error decreases to 4% and 1% which are reduced by 16% and 9%. For defects in SP2 marked as 4 and 8, the error reduced by 13.3% and 8%, respectively. For certain defects with errors of less than 5%, the improvement of errors is relatively small.

From 22 cases of Fig. 10(b) and Table 2, there exist 6 cases with no improvement and 3 of them have the worse impact. This is because of their relatively low nonlinearity degree since the different thermal diffusivity in different materials. However, compared with other cases, these error range does not exceed 2% which the performance is acceptable. The results show that the proposed modified non-linear model can accurately predict the value of  $d$ .

In order to compare with the research works in-depth retrieval by using neural networks [46,47], experimental and simulated data of SP1 were both used to evaluate the method. The original network employs a deep feed-forward networks (DFF) network with five hidden layers, the succeeding hidden layers have two-thirds the number of nodes of that from the preceding layer. In this paper, the network was trained at a learning rate of 0.007 and 5000 iterations with early stopping, which means if the loss of the validation data does not decrease smaller than 0.0001 in 50 epochs, the program will be early stopped. Apart from this, during the NN training through the backpropagation, the Adam optimizer is set up with learning rate of 0.007 and lower bound on the

learning rate is set as  $1 \times 10^{-6}$ . These operations can accelerate the training speed, helping the network convergence and preventing the gradient explosion. The learning system uses ReLU activation function for the hidden layers with a linear activation function for the output layer. Mean square error was selected as the cost function. The batch size (B) is set to 16. The details of the DFF network are shown in Table 3.

The experimental data were first shuffled and divided such that 80% of it was used to train the developed NN while the remaining 20% was used for testing the accuracy of the NN. As shown in Fig. 12, when selecting five locations per defect, a total number of 40 contrast curves will be obtained, 32 curves were used in the training process and the remaining 8 were used for testing. Table 4 illustrates the results and the procedure.

From Table 4, the mean of 5-fold cross-validated accuracy is around 80%. However, the training time is longer. In order to effectively verify the applicability of this method. A CFRP sample SP1 was modeled in COMSOL. The simulation data was used to train the developed NN while the experimental data was used for testing the accuracy of the NN. The 40 points marked in Fig. 13(a) are used for training, and the corresponding 40 experimental points in Fig. 12(a) are used for testing. The predictive accuracy is shown in Table 5.

As shown in Table 5, the accuracy is only 42% since using the simulation data training results to test the experimental data. In conclusion, this approach in depth retrieval by using neural networks can only guarantee the accuracy within certain condition and the training time cost high. The proposed method has ability to process defects in a relatively faster processing computation and does not require any prior training information. In addition, it can treat different CFRP samples.

#### 4. Conclusion and future work

Determination of defect depth by Optical pulsed thermography has been an important research topic. At present, in the time domain, the prediction of defect depth is based on the selection of characteristic time. This paper proposes to use gaussianization transform to determine uncertain value  $\varepsilon$  to correct contrast peak time  $\tau_m$ . The actual physical non-linear relationship between defect depth and contrast peak time is transformed into a linear projection. Quantitative analysis of experimental data can prove the superiority of the proposed transformation. The experimental results indicated that the corrected linear relationship can more accurately determine the defect depth. Future work will focus

**Table 4**  
The accuracy for the defects in the SP1.

#of hidden lays	Training time (s)	Prediction time (ms)	Accuracy (%)
5	30	5	80

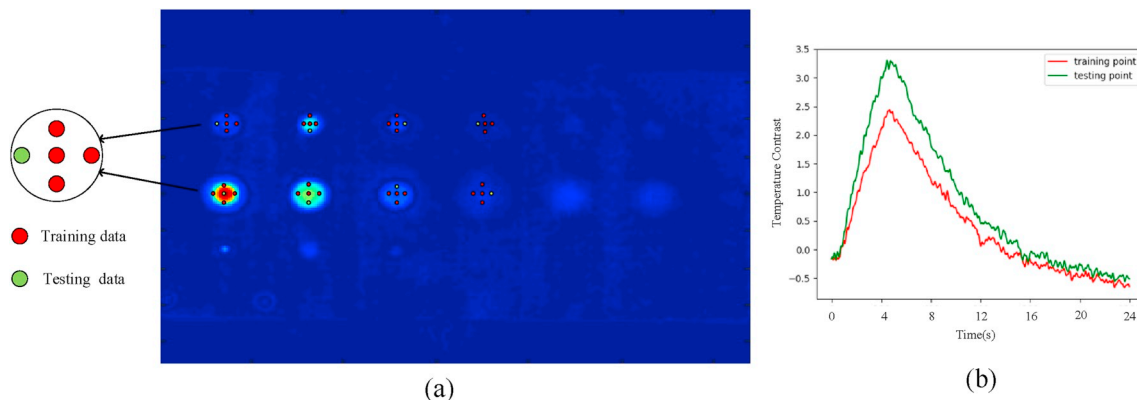


**Fig. 12.** (a) Locations on defects from which temperature curves are extracted (b) Temperature contrasts of the training point and testing point at a depth of 0.5 mm.

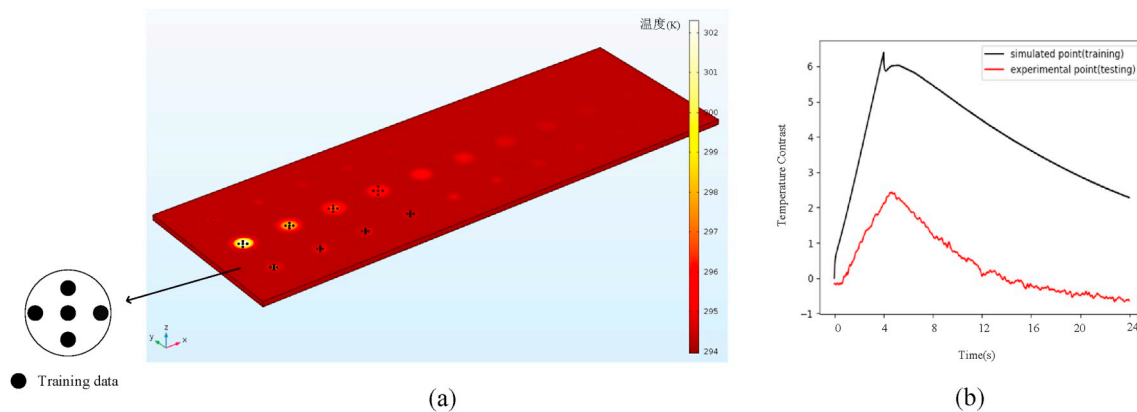


Fig. 13. (a) The CFRP sample SP1 modeled in COMSOL (b) Temperature contrasts of the simulated (training) point and experimental (testing) point at a depth of 0.5 mm.

Table 5

The results of the predictive accuracy.

#of hidden lays	Training time (s)	Prediction time (ms)	Accuracy (%)
5	34	5	42

on definite non-linear factors to determine the specific expression between defect depth and exact peak contrast time by combining the properties of the material.

#### Acknowledgement

The work was supported by National Natural Science Foundation of China (No. 61971093, No. 61527803, No. 61960206010). The work was supported by Science and Technology Department of Sichuan, China (Grant No.2019YJ0208, Grant No.2018JY0655, Grant No. 2018GZ0047) and Fundamental Research Funds for the Central Universities (Grant No. ZYGX2019J067).

#### References

- [1] W.J. Cantwell, J. Morton, The impact resistance of composite materials—a review, *Composites* 22 (5) (1991) 347–362.
- [2] K. Wang, B. Young, S.T. Smith, Mechanical properties of pultruded carbon fibre-reinforced polymer (CFRP) plates at elevated temperatures, *Eng. Struct.* 33 (7) (2011) 2154–2161.
- [3] J. Guo, X. Gao, E. Toma, et al., Anisotropy in carbon fiber reinforced polymer (CFRP) and its effect on induction thermography, *Ndt & E Int.* 91 (2017) 1–8.
- [4] G. Qin, et al., Effect of continuous high temperature exposure on the adhesive of epoxy adhesive, CFRP and adhesively bonded CFRP/aluminum alloy joints, *Compos. Part B* 154 (2018) 43–55.
- [5] F.P. Miller, A.F. Vandome, J. Mcbrewster, *Carbon Fiber-Reinforced Polymer*, Alphascript Publishing, 2011.
- [6] H. Kaczmarek, Ultrasonic detection of the development of transverse cracking under monotonic tensile loading, *Compos. Sci. Technol.* 46 (1) (1993) 67–75.
- [7] B.R. Tittmann, Ultrasonic inspection of composites, *Compr. Compos. Mater.* II 7 (2018) 195–249.
- [8] I. Amenabar, Comparison and analysis of non-destructive testing techniques suitable for delamination inspection in wind turbine blades, *Compos. B Eng.* 42 (5) (2011) 1298–1305.
- [9] A.G. Stamopoulos, K.I. Tserpes, A.J. Dentsoras, Quality assessment of porous CFRP specimens using x-ray computed tomography data and artificial neural network, *Compos. Struct.* 192 (2018) 327–335.
- [10] M.P. De Goeje, K.E.D. Wapenaar, Non-destructive inspection of carbon fibre-reinforced plastics using eddy current method, *Composites* 23 (3) (1992) 147–157.
- [11] G. Mook, R. Lange, O. Koeser, Non-destructive characterization of carbon-fibre-reinforced plastics by means of eddy-current, *Compos. Sci. Technol.* 61 (6) (2001) 865–873.
- [12] A.S. Bin Sediq, N. Qaddoumi, Near-field microwave image formation of defective composites utilizing open-ended waveguides with arbitrary cross sections, *Compos. Struct.* 71 (3–4) (2005) 343–348.
- [13] J.M. Park, S.I. ee, K.L. De Vries, Nondestructive sensing evaluation of surface modified single-carbon fiber reinforced epoxy composites by electrical resistivity measurement, *Compos. B Eng.* 37 (7–8) (2006) 612–626.
- [14] J.M. Park, P.G. Kim, J.H. Jang, et al., Self-sensing and dispersive evaluation of single carbon fiber/carbon nanotube(CNT)-epoxy composites using electro-micromechanical technique and nondestructive acoustic emission, *Comp. Part: Eng.* 39 (7–8) (2008) 1170–1182.
- [15] E.Z. Kordators, D.G. Aggelis, T.E. Matikas, Monitoring mechanical damage in structural materials using complimentary NDE techniques based on thermography and acoustic emission, *Compos. B Eng.* 2012 (43) (2012) 2676–2686.
- [16] C. Garnier, M.L. Pastor, F. Eyma, et al., The detection of aeronautical defects in situ on composite structures using Non Destructive Testing, *Compos. Struct.* 93 (5) (2011) 1328–1336.
- [17] J.A. Schroeder, T. Ahmed, B. Chaudhry, et al., Non-destructive testing of structural composites and adhesively bonded composite joints: pulsed thermography, *Compos. Appl. Sci. Manuf.* 33 (11) (2002) 1511–1517.
- [18] K.H. Lyle, E.L. Fasanella, Permanent set of the space shuttle thermal protection system reinforced carbon-carbon material, *Compos. Appl. Sci. Manuf.* 40 (6–7) (2009) 702–708.
- [19] S. Sfarra, C. IbarraCastanedo, N.P. Avdelidis, et al., A Comparative Investigation for the Nondestructive Testing of Honeycomb Structures by Holographic Interferometry and Infrared thermography[C], 2009.
- [20] P. Theodorakeas, C. Ibarra-Castanedo, S. Sfarra, et al., NDT inspection of plastered mosaics by means of transient thermography and holographic interferometry, *NDT & E Int.* 47 (none) (2012) 150–156.
- [21] R. Gade, T.B. Moeslund, Thermal cameras and applications: a survey, *Mach. Vis. Appl.* 25 (2014) 245–262.
- [22] Y. Duan, S. Huebner, U. Hassler, A. Osman, C. Ibarra-Castanedo, et al., Quantitative evaluation of optical lock-in and pulsed thermography for aluminum foam material, *Infrared Phys. Technol.* 60 (5) (2013) 275–280.
- [23] G.P.M. Fierro, D. Ginzburg, F. Ciampa, M. Meo, Nonlinear ultrasonic stimulated thermography for damage assessment in isotropic fatigued structures, *J. Sound Vib.* 404 (2017) 102–115.
- [24] A. Foudazi, K.M. Donnell, M.T. Ghasr, Application of active microwave thermography to delamination detection, in: 2014 IEEE International Instrumentation and Measurement Technology Conference (I2MTC) Proceedings, IEEE, 2014, May, pp. 1567–1571.
- [25] L. Cheng, G.Y. Tian, Surface crack detection for carbon fiber reinforced plastic (CFRP) materials using pulsed eddy current thermography, *IEEE Sens. J.* 11 (12) (2011) 3261–3268.
- [26] A.O. Chulkov, V.P. Vavilov, *Hardware and Software for Thermal Nondestructive Testing of Metallic and Composite Materials*, 2016, pp. 1392–1397.
- [27] C. Ibarra-Castanedo, D. Gonzalez, M. Klein, M. Pilla, S. Vallerand, X. Maldague, Infrared image processing and data analysis, *Infrared Phys. Technol.* 46 (2004) 75–83.
- [28] Rubén Usamentiaga, P. Venegas, J. Guerediaga, et al., Infrared thermography for temperature measurement and non-destructive testing, *Sensors* 14 (7) (2014) 12305–12348.
- [29] C. Ibarra-Castanedo, *Quantitative Subsurface Defect Evaluation by Pulsed Phase Thermography: Depth Retrieval with the Phase*, University of Laval, Canada, 2005.
- [30] H.I. Syed, K.E. Cramer, Corrosion detection in aircraft skin, *Proc. SPIE* (1993) 160–165, 1933, Thermosense XV.
- [31] S. Sfarra, S. Perilli, D. Paoletti, D. Ambrosini, Ceramics and defects: infrared thermography and numerical simulations -A wide-ranging view for quantitative analysis, *J. Therm. Anal. Calorim.* 123 (1) (2016) 43–62.
- [32] Z. Zeng, C. Li, N. Tao, L. Feng, C. Zhang, Depth prediction of non-air interface defect using pulsed thermography, *NDT E Int.* 48 (2012) 39–45.
- [33] D.P. Almond, P.M. Patel, *Photothermal Science and Techniques*, first ed., Chapman & Hall, London, UK, 1996, ISBN 978-0-412-57880-9.
- [34] S.K. Lau, D.P. Almond, J.M. Milne, A quantitative analysis of pulsed video thermography, *NDT E Int.* 24 (1991) 195–202.
- [35] J.G. Sun, Analysis of pulsed thermography methods for defect depth prediction, *J. Heat Transf.* 128 (4) (2006) 329.
- [36] J.-C. Krapez, F. Lepoutre, D. Balageas, Detection of early contrast in pulsed stimulated thermography, *J. Phys.* III 4 (1994) C7–C47.

- [37] J.C. Krapez, D. Balageas, A. Deom, F. Lepoutre, Early detection by stimulated infrared thermography. Comparison with ultrasonics and holo/shearography, in: X. P.V. Maldague (Ed.), *Advances in Signal Processing for Nondestructive Evaluation of Materials*, vol. 262, Springer, Dordrecht, the Netherlands, 1994, ISBN 978-94-011-1056-3, pp. 303–321.
- [38] Ringermacher, H. I., Archacki, Jr, R. J., and Veronesi, W. A., 1998, "Nondestructive testing: transient depth thermography," U.S. Patent No. 5,711,603.
- [39] Maria K. Theodorakeas, Depth retrieval procedures in pulsed thermography: remarks in time and frequency domain analyses, *Appl. Sci.* 8 (3) (2018) 409.
- [40] S.M. Shepard, J.R. Lhota, B.A. Rubadeux, D. Wang, T. Ahmed, Reconstruction and enhancement of active thermographic image sequences, *Opt. Eng.* 42 (2003) 1337–1342.
- [41] Sun JG. Method for determining defect depth using thermal imaging. US Patent no. 6,542,849, 2003.
- [42] Y. Zhao, J. Mehnen, A. Sirikham, et al., A novel defect depth measurement method based on Nonlinear System Identification for pulsed thermographic inspection, *Mech. Syst. Signal Process.* 85 (2017) 382–395.
- [43] P. Wei, W. Fei, M. Xiang-Lin, et al., Dynamic thermal tomography based on continuous wavelet transform for debonding detection of the high silicon oxygen phenolic resin cladding layer, *Infrared Phys. Technol.* 92 (2018) 115–121.
- [44] M. Omar, M.I. Hassan, K. Saito, et al., IR self-referencing thermography for detection of in-depth defects, *Infrared Phys. Technol.* 46 (4) (2005) 283–289.
- [45] G. Saon, S. Dharanipragada, D. Povey, Feature Space Gaussianization, *IEEE International Conference on Acoustics*, 2004.
- [46] N. Saeed, M.A. Omar, et al., Automatic defects detection in CFRP using convolutional neural networks and transfer learning, *J. Infrared Phys. Technol.* 102 (2019).
- [47] N. Saeed, M.A. Omar, et al., Sensitivity and robustness of neural networks for defect-depth estimation in CFRP Thermograms, *J. Nondestruct. Eval.* 38 (3) (2019) 38–74. Springer Nature.